Mixed-mode fatigue crack growth using cohesive zone modeling

Habeun Choi[a], Kyoungsoo Park[a,*], Glaucio H. Paulino[b]

[a] *Department of Civil & Environmental Engineering, Yonsei University, 50 Yonsei-ro, Seodaemun-gu, Seoul 120-749, Republic of Korea*
[b] *School of Civil & Environmental Engineering, Georgia Institute of Technology, 790 Atlantic Dr., Atlanta, GA 30332, USA*

A B S T R A C T

In order to capture nonlinear crack tip behavior and account for mixed-mode fatigue crack growth, a cohesive zone based fatigue crack growth model is proposed in conjunction with the Park-Paulino-Roesler (PPR) traction-separation relationship. The model clearly defines five stages during arbitrary fatigue loading: softening, unloading, reloading, contact, and complete failure. The cohesive traction-separation relationship is based on the PPR fracture potential, while the fatigue damage is accumulated by introducing two conjugate damage measures. One damage measure is associated with the rate of separation, while the other is related to the rate of traction (or local stress). Additionally, two model constants are introduced to control the normal contact condition, which may be associated with physical conditions such as crack closure, crack face roughness, and oxidation of fracture surface. Furthermore, computational simulations of the proposed fatigue crack growth model are performed for a simple mode-I test, double cantilever beam test, modified mixed-mode bending test, and three-point bending test. The observed computational results lead to stable and consistent fatigue crack growth.

1. Introduction

Fatigue damage may lead to unexpected failure phenomena, such as those observed in infrastructure, because the driving force for fatigue crack growth can be significantly lower than the required driving force under monotonic loading condition. Fatigue crack growth behavior is usually described by a class of relationships that are based on the original phenomenological Paris equation [28], which is the relationship between the fatigue crack growth rate (da/dN) and the amplitude of the applied stress intensity factor (ΔK), i.e., $da/dN = C_1(\Delta K)^{C_2}$. We denote a as the crack length, N as the number of cycles, and C_1 and C_2 as the parameters associated with material properties, geometry, environment, frequency, etc. Based on linear elastic fracture mechanics, fatigue crack growth has been extensively investigated for various engineering applications, e.g., [45,25,34,41,48,49,14,24,55,7]. However, the original Paris relation has limitations, especially when ideal conditions, including linear elastic fracture mechanics, small-scale yielding, long cracks, etc., are not satisfied [54].

As an alternative to the standard Paris relation, the cohesive zone modeling approach has been employed to predict fatigue crack growth, e.g. [9,26,37,36,50,4]. However, previous fatigue crack growth models with the cohesive zone modeling approach display several limitations, as discussed in Section 2. For instance, to account for arbitrary loading amplitude and frequency, some of the model parameters need to be calibrated in relation with the number of cycles and loading ratios. Although fatigue damage may occur when the local stress is lower than the cohesive strength, most models are unable to introduce fatigue damage (without defining the cohesive surface). This is because damage evolution is generally associated with the rate of cohesive separation along the potential fracture surface, and thus damage evolution is not possible unless cohesive surface elements are inserted in the domain.
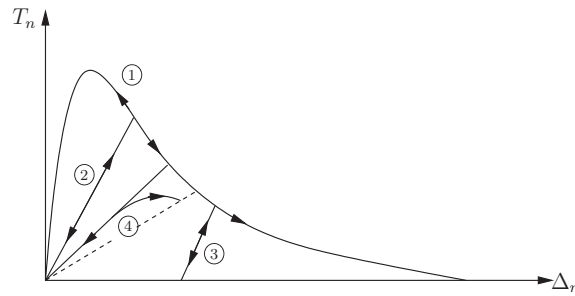

Fig. 1. Illustration of various unloading–reloading relations.

In the present study, a mixed-mode cohesive zone based fatigue crack growth model is proposed in order to account for arbitrary quasi-static cyclic loading history. The proposed model is based on two damage measures associated with the rate of separation and the rate of traction, which provide flexibility in capturing fatigue crack growth behavior. The proposed model is evaluated by solving mode-I and mixed-mode examples with low-cycle fatigue cases. The remainder of the paper is organized as follows. Section 2 briefly reviews previous fatigue crack growth models, which are based on the cohesive zone modeling approach, while addressing their limitations. Next, the proposed fatigue crack growth model is presented in Section 3, and computational examples are provided in Section 4. Finally, the paper is summarized with key findings in Section 5.

2. Related works: previous fatigue crack growth models

To account for nonlinear fracture process in fatigue cracking growth, the cohesive zone model has been employed [9,37]. Usually, fatigue crack growth is represented by defining a fatigue damage variable (D) in the cohesive zone model. The rate of fatigue damage is generally defined using two approaches, i.e., the envelope load damage models, and the hysteresis unloading–reloading damage models. In the envelope load models, e.g., [36,20,10,11], only the maximum load of each load cycle is computed when the damage evolution is directly defined on the basis of the number of cycles (dD/dN). Additionally, some of the envelope load models provide direct relations to the Paris law parameters [47,17,12].

Alternatively, the damage evolution ($\dot{D}$) during cyclic loading is directly computed in conjunction with an unloading–reloading relation in the cohesive zone model, which is the choice of present study. In the literature, few unloading–reloading models were proposed in relation with fatigue damage evolution, e.g., [9,26,37]. If one does not consider an unloading–reloading relation, for example, the cohesive traction may increase during unloading, as described in Path ① of Fig. 1. In order to account for fatigue crack growth, Andres et al. [9] employed a linear unloading–reloading relation, which points towards the origin (Path ② in Fig. 1), in conjunction with conventional continuum plasticity. Deshpande et al. [13] modified the unloading–reloading slope (or stiffness), which resulted in residual opening associated with oxide layer of new surface (Path ③ in Fig. 1). Notice that both models provide the same unloading path as the reloading path, while the envelope of the traction-separation relation does not change. Thus, fatigue damage cannot be introduced within an elastic domain.

In order to demonstrate *hysteresis during unloading and reloading*, the reloading stiffness is generally degraded with a fixed unloading stiffness. For example, Nguyen et al. [26] decreased the reloading stiffness based on the rate of local separation while fixing the unloading stiffness (i.e. linear to the origin), as shown in Path ④ of Fig. 1. Then, the reloading stiffness was approximated with respect to the number of cycles under the uniform separation condition. Later, Maiti and Geubelle [22,23] extended the model by Nguyen et al. [26] to have two internal parameters which were calibrated on the basis of the classical Paris' fatigue curve. Nojavan et al. [27] calibrated fatigue parameters using simple mode-I and mode-II tests, and a cycle jump strategy is employed to investigate high-cycle fatigue examples.

Alternatively, the rate of damage is defined in terms of the rate of separation ($\dot{\Delta}$), and a damage variable is introduced in the traction-separation relationship. Roe and Siegmund [37] proposed an expression for the fatigue damage evolution using the rate of the effective separation in conjunction with the exponential potential-based model [53]. The slope of an unloading path was selected as the initial slope of the derivatives of the exponential potential, which was similar to the model by Deshpande et al. [13]. Similarly, Ural et al. [50] also defined fatigue damage evolution based on the rate of separation, and developed a damage-based cohesive traction-separation relationship. One should note that fatigue damage was not introduced when a separation was smaller than a critical separation whose cohesive traction corresponds to the cohesive strength. This is because the initial ascending region in the traction-separation relationship is considered as artificial compliance.

Based on the damage evolution expression by Roe and Siegmund [37], Jha and Banerjee [18] demonstrated typical stress-life responses under variable amplitude loads, and Li et al. [21] investigated fatigue crack growth under mixed-mode loading conditions. To control damage rate according to a current damage state, Bouvard et al. [6] and Roth et al. [39] introduced power-law terms in the damage evolution. Additionally, because of high computational cost for fatigue analysis, fatigue damage per each cycle is approximated by introducing an extrapolation technique [5,6,16] and a frequency-dependent material parameter [42]. Fatigue crack growth simulation has been extensively performed, and the aforementioned references are only an incomplete sample.

In most previous cohesive zone based fatigue models, fatigue damage is accumulated only when cohesive separation changes. Therefore, when cohesive separation is not specified in a continuum domain, the damage accumulation is not possible. For instance,

although local stress reaches 50% of cohesive strength for millions of times, no fatigue damage is expected if no cohesive surface exists in the finite element discretization. In addition, when the fatigue damage evolution is evaluated in conjunction with the number of cycles, some of the model parameters may be recalibrated with respect to the loading frequencies and/or magnitudes. In order to tackle these limitations of previous models, in this study, a mixed-mode fatigue crack growth model is proposed on the basis of the rate of separation and the rate of traction, as described in the following section.

3. Cohesive zone-based fatigue crack growth

A mixed-mode fatigue crack growth model is proposed in conjunction with a potential-based cohesive zone model and an unloading–reloading relationship. The evolution of fatigue damage is introduced on the basis of five separation states and two damage measures for each fracture mode. In the following subsections, a potential-based cohesive zone model is briefly reviewed. Then, separation states are described using separation variables, and damage measures are introduced in conjunction with the rate of separation and the rate of traction (or stress). Finally, a mixed-mode fatigue traction-separation relationship is presented for arbitrary fatigue loading.

3.1. PPR cohesive zone model: A brief overview

A potential-based cohesive zone model provides a consistent traction-separation relationship for cohesive fracture [33,31,29]. The potential (Ψ) for cohesive fracture is expressed as

$$\Psi(\Delta_n, \Delta_t) = \min(\phi_n, \phi_t) + \left[\Gamma_n\left(1 - \frac{\Delta_n}{\delta_n}\right)^\alpha\left(\frac{m}{\alpha} + \frac{\Delta_n}{\delta_n}\right)^m + \langle\phi_n - \phi_t\rangle\right]\left[\Gamma_t\left(1 - \frac{|\Delta_t|}{\delta_t}\right)^\beta\left(\frac{n}{\beta} + \frac{|\Delta_t|}{\delta_t}\right)^n + \langle\phi_t - \phi_n\rangle\right]$$

(1)

where Δ_n and Δ_t are normal and tangential separations, respectively, and $\langle\cdot\rangle$ is the Macaulay bracket. Due to the nature of the potential, the derivatives of the potential with respect to normal and tangential separations lead to the normal and tangential cohesive tractions, i.e.,

$$\frac{\partial\Psi(\Delta_n, \Delta_t)}{\partial\Delta_n} = \frac{\Gamma_n}{\delta_n}\left[m\left(1 - \frac{\Delta_n}{\delta_n}\right)^\alpha\left(\frac{m}{\alpha} + \frac{\Delta_n}{\delta_n}\right)^{m-1} - \alpha\left(1 - \frac{\Delta_n}{\delta_n}\right)^{\alpha-1}\left(\frac{m}{\alpha} + \frac{\Delta_n}{\delta_n}\right)^m\right]\left[\Gamma_t\left(1 - \frac{|\Delta_t|}{\delta_t}\right)^\beta\left(\frac{n}{\beta} + \frac{|\Delta_t|}{\delta_t}\right)^n + \langle\phi_t - \phi_n\rangle\right],$$

(2)

and

$$\frac{\partial\Psi(\Delta_n, \Delta_t)}{\partial\Delta_t} = \frac{\Gamma_t}{\delta_t}\left[n\left(1 - \frac{|\Delta_t|}{\delta_t}\right)^\beta\left(\frac{n}{\beta} + \frac{|\Delta_t|}{\delta_t}\right)^{n-1} - \beta\left(1 - \frac{|\Delta_t|}{\delta_t}\right)^{\beta-1}\left(\frac{n}{\beta} + \frac{|\Delta_t|}{\delta_t}\right)^n\right]\left[\Gamma_n\left(1 - \frac{\Delta_n}{\delta_n}\right)^\alpha\left(\frac{m}{\alpha} + \frac{\Delta_n}{\delta_n}\right)^m + \langle\phi_n - \phi_t\rangle\right]\frac{\Delta_t}{|\Delta_t|}.$$

(3)

Characteristic parameters (Γ_n, Γ_t, δ_n, δ_t, m, n, α, β) are evaluated on the basis of cohesive fracture properties such as fracture energy (ϕ_n, ϕ_t), cohesive strength ($\sigma_{\max}$, $\tau_{\max}$), initial slope, and shape of the traction-separation relationship. When the normal fracture energy (ϕ_n) is different from the tangential fracture energy (ϕ_t), the energy constants (Γ_n, Γ_t) are given as

$$\Gamma_n = (-\phi_n)^{\frac{\langle\phi_n-\phi_t\rangle}{\phi_n-\phi_t}}\left(\frac{\alpha}{m}\right)^m, \quad \Gamma_t = (-\phi_t)^{\frac{\langle\phi_t-\phi_n\rangle}{\phi_t-\phi_n}}\left(\frac{\beta}{n}\right)^n \quad \text{for } (\phi_n \neq \phi_t)$$

(4)

For the same fracture energy, the energy constants are expressed as

$$\Gamma_n = -\phi_n\left(\frac{\alpha}{m}\right)^m, \quad \Gamma_t = \left(\frac{\beta}{n}\right)^n \quad \text{for } (\phi_n = \phi_t).$$

(5)

The nondimensional exponents (m, n) are determined as

$$m = \frac{\alpha(\alpha - 1)\lambda_n^2}{(1 - \alpha\lambda_n^2)}, \quad n = \frac{\beta(\beta - 1)\lambda_t^2}{(1 - \beta\lambda_t^2)}$$

(6)

where the initial slope indicators (λ_n, λ_t) correspond to the ratio of a critical crack opening width to a final crack opening width (i.e., $\lambda_n = \delta_{nc}/\delta_n$ and $\lambda_t = \delta_{tc}/\delta_t$). Note that a critical crack opening width (δ_{nc}, δ_{tc}) is separation, which results in the maximum cohesive traction, i.e. the cohesive strength ($\sigma_{\max}$, $\tau_{\max}$). A final crack opening width (δ_n, δ_t), also named as a complete separation, is separation where the cohesive traction becomes zero. The final crack opening widths (δ_n, δ_t) are given as

$$\delta_n = \frac{\phi_n}{\sigma_{\max}}\alpha\lambda_n(1 - \lambda_n)^{\alpha-1}\left(\frac{\alpha}{m} + 1\right)\left(\frac{\alpha}{m}\lambda_n + 1\right)^{m-1}$$

(7)

$$\delta_t = \frac{\phi_t}{\tau_{\max}}\beta\lambda_t(1 - \lambda_t)^{\beta-1}\left(\frac{\beta}{n} + 1\right)\left(\frac{\beta}{n}\lambda_t + 1\right)^{n-1}.$$

(8)

In addition, α and β are shape parameters, which handle the shape of the traction-separation relation, e.g. linear, convex, or concave.

The normal and tangential traction-separation relationships [Eqs. (2) and (3)] are defined within the normal and tangential interaction regions, respectively. When separation is outside of the interaction region, the corresponding cohesive traction is zero.

The normal and tangential interaction regions are defined using the complete separation (δ_n, δ_t) and the conjugate complete separation ($\bar{\delta}_n$, $\bar{\delta}_t$). One notes that $\bar{\delta}_n$ and $\bar{\delta}_t$ are evaluated by solving the following nonlinear equations:

$$f_n(\Delta_n) = \Gamma_n \left(1 - \frac{\Delta_n}{\delta_n}\right)^\alpha \left(\frac{m}{\alpha} + \frac{\Delta_n}{\delta_n}\right)^m + \langle \phi_n - \phi_t \rangle \tag{9}$$

and

$$f_t(\Delta_t) = \Gamma_t \left(1 - \frac{|\Delta_t|}{\delta_t}\right)^\beta \left(\frac{n}{\beta} + \frac{|\Delta_t|}{\delta_t}\right)^n + \langle \phi_t - \phi_n \rangle, \tag{10}$$

respectively.

The potential-based model accounts for cohesive failure under monotonic loading (or separation) condition. Thus, energy dissipation during cyclic loading is considered in conjunction with a traction-separation relationship under the unloading and reloading conditions.

3.2. Separation states

A mixed-mode fatigue traction-separation relationship is defined on the basis of five separation states and two damage measures for each fracture mode. The five separation states consist of softening, unloading, reloading, contact, and complete failure conditions. The softening condition is defined when a material displays progressive separation due to monotonic external boundary conditions. If one releases the external boundary conditions, the separation monotonically decreases. Such condition is defined as the unloading condition. When the external boundary conditions are applied again, the separation increases, which leads to the reloading condition. Additionally, the complete failure condition is defined when the cohesive traction becomes zero, while the mode-I contact condition occurs when the crack face closes.

Under mixed-mode, the five separation states are determined by means of the following separation variables: complete separations (δ_n, δ_t), conjugate complete separations ($\bar{\delta}_n$, $\bar{\delta}_t$), boundary separations (δ_{nb}, δ_{tb}), normal contact separation (δ_{no}), and rate of separations ($\dot{\Delta}_n$, $\dot{\Delta}_t$). The normal interaction region is defined within $0 \leqslant \Delta_n \leqslant \delta_n$ and $|\Delta_t| \leqslant \bar{\delta}_t$ [see Fig. 2(a)], while the tangential
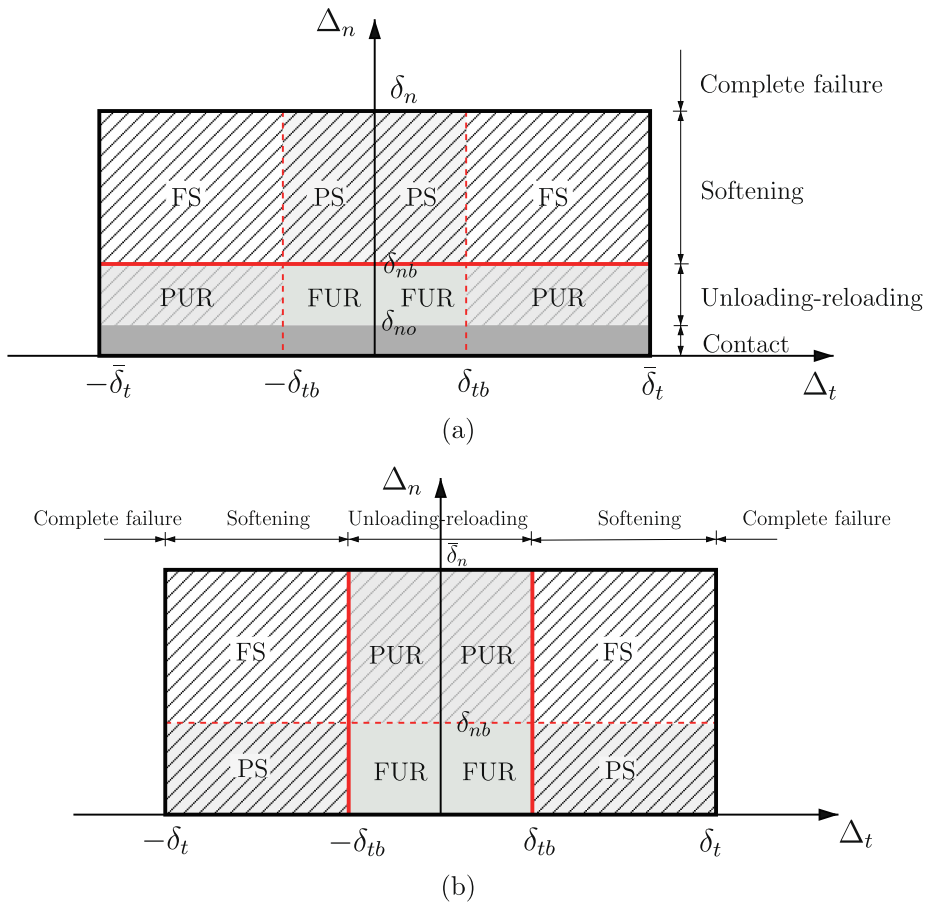

Fig. 2. Separation states for (a) normal interaction region, and (b) tangential interaction region. Full softening (FS), partial softening (PS), full unloading–reloading (FUR), and partial unloading–reloading (PUR) are defined in the cohesive interaction regions.

interaction region corresponds to $0 \leqslant \Delta_n \leqslant \bar{\delta}_n$ and $|\Delta_t| \leqslant \delta_t$ [see Fig. 2(b)]. When the separation is outside of the interaction region, the cohesive traction becomes zero, i.e., no bearing capacity, which leads to the complete failure condition. The normal complete failure condition is when $\Delta_n \geqslant \delta_n$ or $|\Delta_t| \geqslant \bar{\delta}_t$; the tangential complete failure condition is when $\Delta_n \geqslant \bar{\delta}_n$ or $|\Delta_t| \geqslant \delta_t$.

The boundary between the softening condition and the unloading–reloading condition is identified by introducing normal and tangential boundary separations (δ_{nb}, δ_{tb}), which correspond to the red thick solid lines in Fig. 2. The boundary separation is initially zero, and monotonically increases up to the complete separation based on the damage measure associated with the rate of separation (D_n^Δ, D_t^Δ), i.e. $\delta_{nb} = D_n^\Delta \delta_n$ and $\delta_{tb} = D_t^\Delta \delta_t$. Note that D_n^Δ and D_t^Δ increase from zero to one through damage accumulation, and thus δ_{nb} and δ_{tb} monotonically increase from zero to δ_n and δ_t, respectively.

The separation state $\delta_{nb} \leqslant \Delta_n \leqslant \delta_n$ provides the normal softening condition in the normal interaction region, while the state $\delta_{tb} \leqslant |\Delta_t| \leqslant \delta_t$ leads to the tangential softening condition in the tangential interaction region, as shown in Fig. 2. The softening condition consists of the two parts, full softening (FS) and partial softening (PS). The FS condition is when both normal and tangential separation states are under the softening condition. The normal (or tangential) PS condition indicates that the normal (or tangential) separation state is under the softening condition while the other state is under the unloading–reloading condition. The normal PS region is where the separation state is $\delta_{nb} \leqslant \Delta_n \leqslant \delta_n$ and $0 \leqslant |\Delta_t| \leqslant \delta_{tb}$; the tangential PS region is where the separation state is $\delta_{no} \leqslant \Delta_n \leqslant \delta_{nb}$ and $\delta_{tb} \leqslant |\Delta_t| \leqslant \delta_t$.

For the unloading–reloading conditions, the separation states in the normal and tangential interaction regions correspond to $\delta_{no} \leqslant \Delta_n \leqslant \delta_{nb}$ and $0 \leqslant |\Delta_t| \leqslant \delta_{tb}$, respectively. The positive rate of separation indicates the reloading condition ($\dot{\Delta}_n > 0$, $\dot{\Delta}_t > 0$), while the negative rate of separation represents the unloading condition ($\dot{\Delta}_n < 0$, $\dot{\Delta}_t < 0$). The unloading–reloading condition is divided into the full unloading–reloading (FUR) and the partial unloading–reloading (PUR), as in the softening condition. When both normal and tangential separation states are under the unloading–reloading condition, the corresponding state is defined as FUR. The separation state is PUR when either normal or tangential separation state is under the unloading–reloading condition while the other state is under the softening condition.

Finally, the separation, which provides closed crack face, is defined as the normal contact separation (δ_{no}). When current normal separation is smaller than the contact separation ($\Delta_n \leqslant \delta_{no}$), i.e., dark gray region in Fig. 2(a), the current state represents the contact condition for the normal interaction region. Under the normal contact condition, the tangential separation state is identified according to the current tangential separation (Δ_t), as shown in Fig. 2(b).

3.3. Evolution of fatigue damage

Fatigue damage accumulation is represented by introducing two damage measures, i.e. one damage associated with the rate of separation ($\dot{\Delta}_n$, $\dot{\Delta}_t$) and the other related to the rate of traction ($\dot{T}_n$, $\dot{T}_t$) for each fracture mode. Most previous researchers (e.g., [37,2,5]) used a damage measure based on the rate of separation. The present study introduces the traction damage measure based on the rate of traction, and proposes that the two damage measures are separately evolved. Because of two types of damage measure, one may expect to have more flexibility on representing fatigue crack growth behavior under various loading conditions.

The fatigue damage measures are initially zero, and evolve based on the following assumptions.

- The increment of damage is associated with the increment of deformation and stress.
- Higher change of deformation and stress results in higher accumulation of fatigue damage.
- Fatigue damage is inverse proportional to fatigue resistance.
- No damage accumulation occurs when the rate of separation or the rate of traction (or stress) is negative.
- Under the normal contact condition, no damage evolution is considered along the normal direction.

Based on the above assumptions, the four damage measures (D_n^Δ, D_t^Δ, D_n^T, D_t^T) monotonically increase from zero to one during cyclic loading. The evolution of damage ($\dot{D}_n^\Delta$, $\dot{D}_t^\Delta$) associated with the rate of separation is defined as

$$\dot{D}_n^\Delta = \begin{cases} \dot{\Delta}_n/\delta_n & \text{for softening} \\ \dot{\Delta}_n/\kappa_n^\Delta \delta_n & \text{for reloading} \\ 0 & \text{for unloading or contact} \end{cases} \tag{11}$$

and

$$\dot{D}_t^\Delta = \begin{cases} \dot{\Delta}_t/\delta_t & \text{for softening} \\ \dot{\Delta}_t/\kappa_t^\Delta \delta_t & \text{for reloading} \\ 0 & \text{for unloading} \end{cases} \tag{12}$$

where κ_n^Δ and κ_t^Δ are the non-dimensional separation rate resistance parameters for fatigue damage along the normal and tangential directions, respectively. Similarly, the rate of the traction (or stress) damage measure ($\dot{D}_n^T$, $\dot{D}_t^T$) is defined as

$$\dot{D}_n^T = \begin{cases} \dot{T}_n/\kappa_n^T \sigma_{max} & \text{for reloading} \\ 0 & \text{for softening, unloading or contact} \end{cases} \tag{13}$$
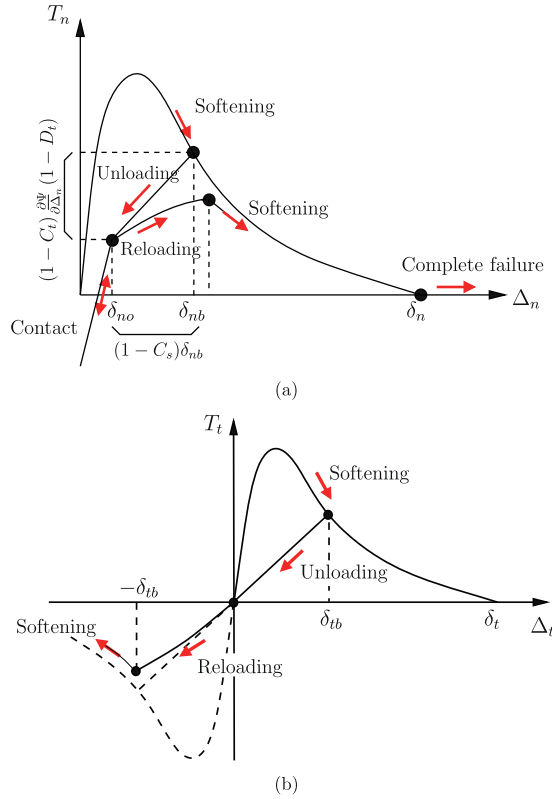
and

Fig. 3. Schematics of the fatigue model for (a) normal traction-separation relationship, and (b) tangential traction-separation relationship.

$$\dot{D}_t^T = \begin{cases} \dot{T}_t/\kappa_t^T \tau_{max} & \text{for reloading} \\ 0 & \text{for softening or unloading} \end{cases} \tag{14}$$

where κ_n^T and κ_t^T are the non-dimensional stress rate resistance parameters for fatigue damage along the normal and tangential directions, respectively. The fatigue resistance parameters (κ_n^Δ, κ_t^Δ, κ_n^T, κ_s^T) are associated with material properties, which control fatigue crack growth. Higher values of the fatigue resistance parameters correspond to more fatigue resistance, and thus slower fatigue crack growth is expected.

3.4. Fatigue traction-separation relationship

In order to represent damage accumulation for arbitrary cyclic loading, a mixed-mode cohesive traction-separation relationship is proposed on the basis of the two damage measures for each fracture mode. The damage (D_n^Δ, D_t^Δ) due to the rate of separation is associated with the unloading–reloading hysteresis relationship, while the damage (D_n^T, D_t^T) due to the rate of traction is related to the envelop of the softening curve. Figs. 3(a) and (b) show the schematics of the normal and tangential traction-separation relationships according to the separation states. First, for the softening condition, the normal and tangential traction-separation relationships are obtained directly from the derivatives of the potential, which are expressed as

$$T_n(\Delta_n, \Delta_t) = \frac{\partial \Psi(\Delta_n, \Delta_t)}{\partial \Delta_n}(1 - D_n^T) \tag{15}$$

and

$$T_t(\Delta_n, \Delta_t) = \frac{\partial \Psi(\Delta_n, \Delta_t)}{\partial \Delta_t}(1 - D_t^T), \tag{16}$$

respectively. Note that D_n^T and D_t^T are initially zero (i.e. no damage), and do not change under the softening condition ($\dot{D}_n^T = \dot{D}_t^T = 0$). Thus, under the monotonic separation, the traction-separation relations [Eqs. (15) and (16)] are the same as the derivatives of the potential [Eqs. (2) and (3)]. However, during cyclic loading (i.e. under the reloading condition), the traction damage measure increases from zero to one, which leads to the decrease of cohesive traction under the softening condition.

For the unloading and reloading conditions, the normal and tangential fatigue traction-separation relationships are defined as

$$T_n(\Delta_n, \Delta_t) = \frac{\partial \Psi(\delta_{nb}, \delta_{tb})}{\partial \Delta_n}(1 - D_n^T)\left(C_t + \frac{1 - C_t}{1 - C_s}\left(\frac{\Delta_n}{\delta_{nb}} - C_s\right)\right)$$ (17)

and

$$T_t(\Delta_n, \Delta_t) = \frac{\partial \Psi(\delta_{nb}, \delta_{tb})}{\partial \Delta_t}(1 - D_t^T)\frac{\Delta_t}{\delta_{tb}}$$ (18)

which result in linear unloading and nonlinear reloading relations, as shown in Fig. 3. For the unloading condition, no damage is accumulated, and thus all damage measures are constant during the unloading condition. Then, the unloading path is linear from the boundary separation to the contact separation for the normal traction [Fig. 3(a)], while the path is linear from the boundary separation to zero for the tangential traction [Fig. 3(b)]. The contact separation is defined by introducing a contact separation ratio (C_s), while the corresponding traction, named as contact traction, is specified using a contact traction ratio (C_t). Note that C_s is the ratio of the contact separation to the boundary separation while C_t is the ratio of the contact traction to the boundary traction. The contact traction and the boundary traction are the cohesive tractions whose corresponding separations are δ_{no} and δ_{nb}, respectively. The values of C_s and C_t can be selected from zero to one. The higher value of C_s leads to the larger contact separation. Similarly, the larger value of C_t results in the larger cohesive traction for the contact separation. For zero C_t and non-zero C_s, a finite separation occurs at the zero traction, which is similar to the previous unloading model by Deshpande et al. [13]. When both C_s and C_t are zero, the unloading path is linear towards the origin, which reproduces the previous unloading model by de Andres et al. [9]. Then, the normal unloading–reloading relationship is simplified as

$$T_n(\Delta_n, \Delta_t) = \frac{\partial \Psi(\delta_{nb}, \delta_{tb})}{\partial \Delta_n}(1 - D_n^T)\frac{\Delta_n}{\delta_{nb}}$$ (19)

which is also analogous to Eq. (18).

For the reloading condition, the reloading stiffness monotonically decreases due to the increase of the four damage measures ($D_n^\Delta, D_t^\Delta, D_n^T, D_t^T$). The separation damage measure (D_n^Δ, D_t^Δ) increases with respect to the increase of the boundary separation (δ_{nb}, δ_{tb}), which results in the decrease of the reloading stiffness. The increase of the cohesive traction damage measure (D_n^T, D_t^T) provides the decrease of the corresponding cohesive traction and the reloading stiffness. Note that when the separation is on the boundary between the softening condition and the unloading–reloading condition ($\Delta_n = \delta_{nb}, \Delta_t = \delta_{tb}$), the cohesive traction obtained from the softening condition [Eqs. (15) and (16)] is the same as the cohesive traction obtained from the unloading–reloading condition [Eqs. (17) and (18)].

Under the normal contact condition, compression acts on the fracture surface. Thus, a penalty stiffness is introduced in the normal traction-separation relationship to prevent from material self-penetration. Additionally, a cohesive frictional-contact model, which accounts for the stick–slip condition, can be utilized for the tangential traction-separation relationship [3]. Finally, for the complete failure condition, the cohesive traction is zero.

One should note that the normal (or tangential) separation state can be under the softening condition, while the tangential (or normal) separation state can be under the unloading–reloading condition, which leads to the normal (or tangential) PS and tangential (or normal) PUR conditions, as discussed in Section 3.2. To consistently handle PS and PUR conditions, a simple coupling procedure proposed by Spring et al. [46] is employed. For the normal PS and tangential PUR conditions, the normal and tangential cohesive tractions are given as

$$T_n(\Delta_n, \Delta_t) = \frac{\partial \Psi(\Delta_n, \delta_{tb})}{\partial \Delta_n}(1 - D_n^T)$$ (20)

and

$$T_t(\Delta_n, \Delta_t) = \frac{\partial \Psi(\Delta_n, \delta_{tb})}{\partial \Delta_t}(1 - D_t^T)\frac{\Delta_t}{\delta_{tb}}$$ (21)

For the normal PUR and tangential PS conditions, the normal and tangential cohesive tractions are expressed as

$$T_n(\Delta_n, \Delta_t) = \frac{\partial \Psi(\delta_{nb}, \Delta_t)}{\partial \Delta_n}(1 - D_n^T)\left(C_t + \frac{1 - C_t}{1 - C_s}\left(\frac{\Delta_n}{\delta_{nb}} - C_s\right)\right)$$ (22)

and

$$T_t(\Delta_n, \Delta_t) = \frac{\partial \Psi(\delta_{nb}, \Delta_t)}{\partial \Delta_t}(1 - D_t^T)$$ (23)

The cohesive tractions for the normal and tangential PS conditions [Eqs. (20) and (23)] are equivalent to the Eqs. (15) and (16) of the FS conditions, while the cohesive tractions for the normal and tangential PUR conditions [Eqs. (22) and (21)] are analogous to the Eqs. (17) and (18) of the FUR conditions.

In summary, when separation initially increases (softening condition), the fatigue traction-separation relationship is obtained from the derivative of the potential (i.e. $D_n^T = D_t^T = 0$). When an external force is unloaded, the cohesive traction linearly decreases while separation decreases. If normal separation is smaller than the contact separation, the stiffness of the traction-separation relation is penalized to prevent from further crack closing. For the reloading condition, the reloading stiffness decreases with respect to the

increase of the damage measures due to fatigue damage. When separation is greater than the boundary separation, the current state changes from the reloading condition to the softening condition. Because of fatigue damage under the reloading condition, the fatigue cohesive traction is lower than the derivative of the potential. If separation is greater than the complete separation, not only is the cohesive traction zero, but the damage associated with the rate of separation becomes one. We remark that one can employ the proposed fatigue damage evolution and unloading-reloading relationship with other cohesive zone models, which describe the envelope of the traction-separation relation.

4. Numerical examples

The proposed fatigue crack growth model is implemented in ABAQUS as a user-defined element (UEL) subroutine [1,30]. In the present study, cohesive surface elements are inserted along the potential crack path when the domain is discretized, which leads to the intrinsic cohesive zone model. In the following subsections, four computational examples are provided: simple mode-I test, double cantilever beam problem, modified mixed-mode bending test, and three-point bending test. A simple mode-I fracture test is introduced to study the effect of model parameters on the fatigue cohesive traction-separation relation. A double cantilever beam and modified mixed-mode bending examples are investigated to observe fatigue crack growth behavior and to compare the proposed model with the Paris relation. Finally, computational simulation of a three-point bending test is compared with experimental fatigue testing results of concrete.

4.1. Simple mode–I test

Effects of the fatigue resistance parameters (κ_n^Δ, κ_n^T) and the contact separation and traction ratios (C_s, C_t) on a fatigue traction-separation relation are investigated by employing a simple mode-I fatigue test. A 0.1 m by 0.1 m square plate is loaded and unloaded along the vertical direction, while a cohesive surface element is inserted at the bottom of the plate. Note that this configuration provides a homogeneous stress state. Material properties are arbitrarily selected. The elastic modulus and the Poisson's ratio are 10.34 MPa and 0.3, respectively, with a unit thickness of the plate. For cohesive fracture properties, the fracture energy is 98.1 N/m, and the cohesive strength is 100 kPa with the shape parameter of 3. The initial slope indicator is selected as a small value (e.g. $\lambda_n = 0.02$) for numerical stability in order to reduce artificial compliance.

The effect of the traction rate resistance (κ_n^T) is first investigated by applying a constant cyclic loading. Here, a constant cyclic loading of 5 kN is applied for twenty times under force control, and then the plate is elongated up to the complete failure under displacement control. The traction resistance parameter (κ_n^T) is selected as 100, 200 and 500 while the separation resistance parameter (κ_n^Δ) is fixed as 10. In addition, the contact separation and traction ratios are set to be zero, i.e. $C_s = 0$ and $C_t = 0$, which leads to a linear unloading towards the origin. The relation between the stress along the vertical direction and the displacement at the top of the plate is plotted in Fig. 4(a). The zoom of the peak load and the cyclic load regions are illustrated in Fig. 4(b). The results from the cyclic loading case are plotted in marked-solid lines while the result from the monotonic loading case is described in a thick solid line. The cyclic loading case results in lower load capacity than the monotonic loading case. In addition, the higher value of the traction rate resistance (κ_n^T) leads to the higher peak load and the higher post-peak load.

We note that if one employs the previous fatigue models (i.e., [37,50]), the peak load and softening behavior for the cyclic loading case will be the same as for the monotonic loading case. This is because the previous fatigue models are unable to introduce fatigue
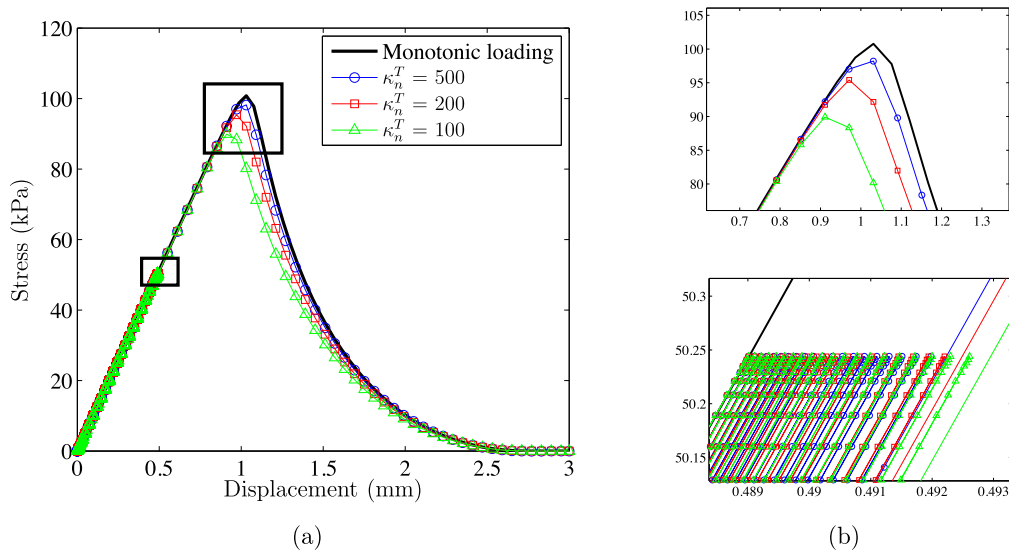

Fig. 4. Effect of the traction rate resistance parameter (κ_n^T) on fatigue damage: (a) stress versus displacement curves, and (b) zooms of the peak load and the cyclic load regions.
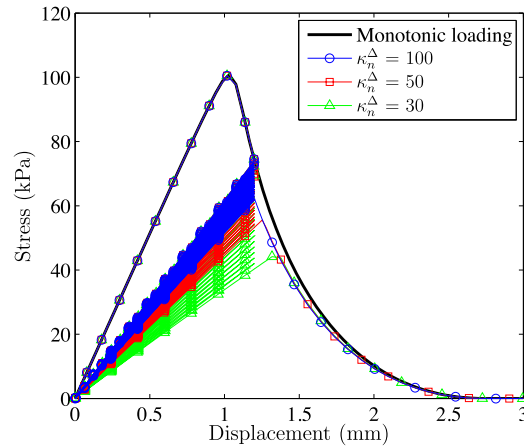
Fig. 5. Effect of the separation rate resistance parameter (κ_n^Δ) on fatigue damage.

damage before the local traction reaches the cohesive strength, which corresponds to the artificial compliance region in the intrinsic cohesive zone model. Alternatively, the fatigue damage can be introduced in the artificial compliance region using the rate of separation [43,40,8]. However, in the intrinsic cohesive zone model, the effect of artificial compliance on computational results should be generally eliminated, and thus an initial ascending slope is usually selected as a large value for numerical stability [33]. Then, the fatigue damage may largely depend on the artificial compliance if the damage evolution model is solely based on the rate of separation. Thus, fatigue damage evolution within this region should be carefully considered in conjunction with artificial compliance.

Next, the effect of the separation rate resistance parameter (κ_n^Δ) is investigated by applying a constant cyclic displacement. The plate is elongated up to 12 mm and released to zero for twenty times, and then it is elongated up to the complete failure. The traction rate resistance parameter is fixed as 200 while the separation rate resistance parameter is chosen as 30, 50 and 100. The contact separation and traction ratios are assumed to be zero. Fig. 5 demonstrates the computational results with respect to the different separation rate resistances. The monotonic loading case is also included in a thick solid line for comparison purpose. The increase of the separation rate resistance results in higher reloading and unloading stiffness in the unloading–reloading relation under the constant displacement amplitude. Additionally, the stress versus displacement curves for the cyclic displacement case are lower than that of the monotonic loading case because of the fatigue damage.

Finally, the effect of the contact separation and traction ratios (C_s, C_t) on the fatigue traction-separation relation is illustrated in Fig. 6. A constant cyclic displacement is applied for twenty times from zero to 12 mm, and then the plate is elongated up to complete failure. The fatigue separation and traction resistance parameters are selected as 30 and 200, respectively. When both contact separation and traction ratios are zero, the unloading path points towards the origin, as shown in Figs. 4(a) and 5. The contact condition is expected when the separation and traction are smaller than zero. With the non-zero contact separation ratio and the zero contact traction ratio [Fig. 6(a)], the contact condition occurs at zero traction with finite separation. The larger value of C_s leads to the increase of separation at the onset of the contact condition. Additionally, the separation at the onset of the contact condition increases during the cyclic displacement loading. For the zero contact separation ratio and the non-zero contact traction ratio, a material contact starts at zero separation with finite traction [Fig. 6(b)]. The increase of C_t results in the higher traction at the onset of the contact traction. For the non-zero contact separation and traction ratios, as expected, the contact condition occurs at non-zero separation and traction [Fig. 6(c)].

4.2. Double cantilever beam test

A double cantilever beam test is employed to investigate the fatigue crack growth and to compare computational results with the Paris relations. The geometry of the double cantilever beam is illustrated in Fig. 7, and a cyclic load (P) of 10 kN is applied. The elastic modulus and the Poisson's ratio are 70 GPa and 0.33, respectively, and the cohesive strength is 6.66 MPa. The geometry and the material properties are taken from an example provided by Ural et al. [50]. Additionally, the fracture energy (ϕ_n) and the cohesive shape parameter (α) are selected as 800 N/m and 3, respectively.

In computational simulation, a crack tip location is defined by employing two approaches [56]. One crack tip corresponds to the final crack opening width (δ_n), called as the macroscopic crack tip. The other location is the critical separation (δ_{nc}), named as the microscopic crack tip, whose cohesive traction corresponds to the maximum in the traction-separation relationship. In addition, the stress intensity factor (K_I) is approximately calibrated on the basis of linear elastic fracture mechanics [15], which is given as

$$K_I = \frac{P}{B\sqrt{h}} \left\{ \sqrt{12}\left(\frac{a}{h} + 0.673\right) + \sqrt{\frac{2h}{\pi a}} - \left(0.815\left(\frac{a}{h}\right)^{0.619} + 0.429\right)^{-1} \right\}$$

(24)

where a is a crack length, and h is a height of each cantilever beam with a unit thickness ($B = 1$). The crack length is calculated by
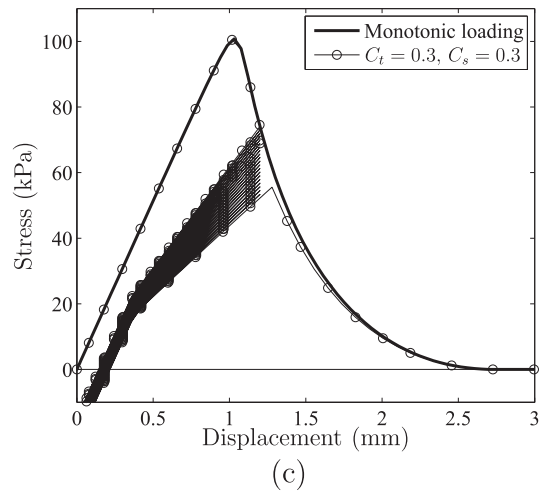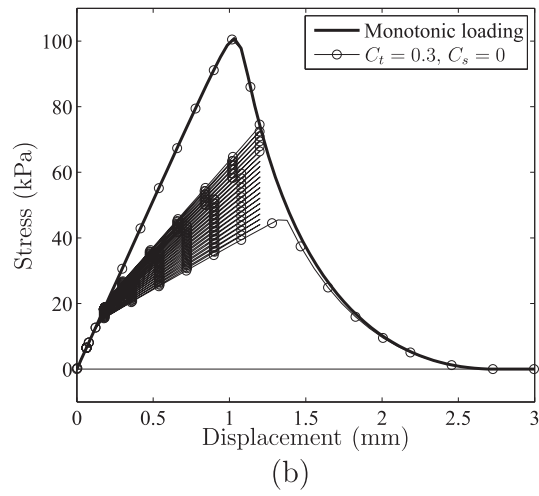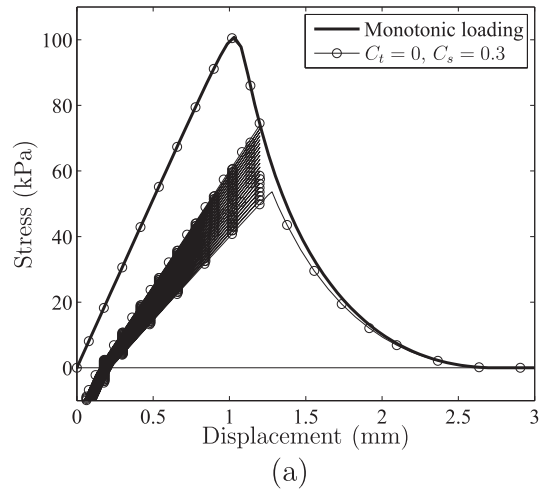
Fig. 6. Effect of the contact separation and traction ratios on fatigue damage: (a) non-zero contact separation ratio, (b) non-zero contact traction ratio, and (c) non-zero contact separation and traction ratios.
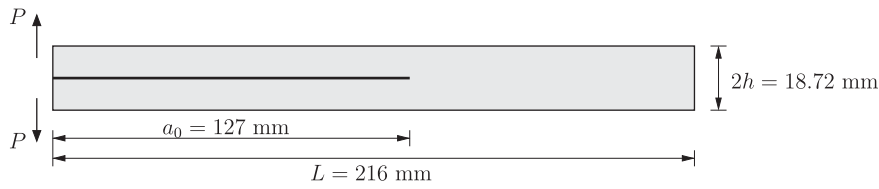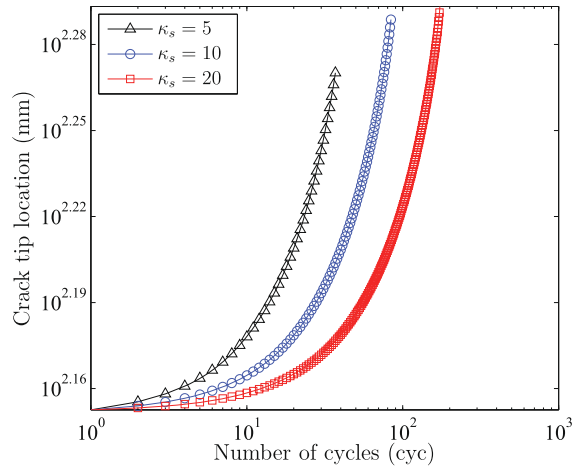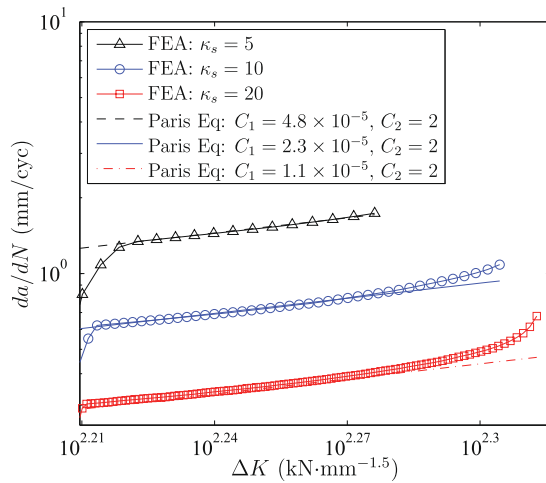
Fig. 7. Geometry of a double cantilever beam.

Fig. 8. Effect of the fatigue separation resistance (κ_n^Δ) on (a) fatigue crack growth and (b) fatigue crack growth rate.

adding the initial crack length (a_0) and the length from the macroscopic crack tip to the initial crack tip.

Then, fatigue crack growth phenomena are simulated by changing the fatigue resistance parameters (κ_n^Δ, κ_n^T) and the cohesive fracture parameters (ϕ_n, $\sigma_{\max}$). The separation resistance parameter (κ_n^Δ) is first arbitrarily selected as 5, 10 and 20 with the given cohesive fracture parameters. The traction resistance parameter is fixed as infinity, which leads to no damage associated with the rate of traction. The relation between the microscopic crack tip position and the number of loading cycles is plotted in Fig. 8(a). The higher separation rate resistance parameter results in higher number of loading cycles for fatigue crack growth, as expected. Additionally, the fatigue crack growth rate (da/dN) versus the stress intensity factor (ΔK_I) curves are plotted in logarithmic scales [Fig. 8(b)]. The da/dN versus ΔK_I curves shift upwards (i.e. faster fatigue crack growth rate) while the separation rate resistance parameter decreases. Additionally, the da/dN versus ΔK_I curves obtained from the computational results are compared with the classical Paris equation. The slope (C_2) is fixed as 2 for a constant traction resistance parameter, while an intercept (C_1) changes with respect to the change of the separation resistance parameter. When the fatigue separation resistance (κ_n^Δ) doubles, the constant (C_1) in
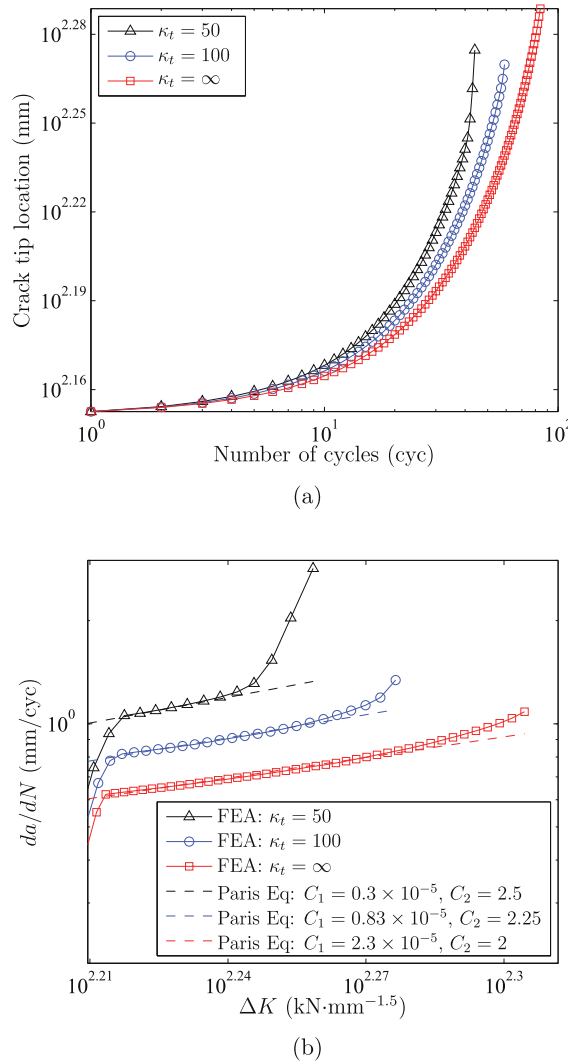
(a)

(b)

Fig. 9. Effect of the fatigue traction resistance (κ_n^T) on (a) fatigue crack growth and (b) fatigue crack growth rate.

the Paris equation decreases almost in half.

Next, the traction resistance parameter (κ_n^T) is selected as 50, 100, and infinity while the separation resistance parameter is fixed as 10 with the given cohesive fracture parameters. Similarly, the increase of κ_n^T results in slower fatigue crack growth, as shown in Fig. 9. For a given number of cycles, the length of the fatigue crack increases with respect to the decrease of the traction resistance parameter [Fig. 9(a)]. In the da/dN versus ΔK_I relation [Fig. 9(b)], the higher value of κ_n^T leads to the slower rate of the fatigue crack growth, which corresponds to the decrease of the slope (C_2) in the classical Paris equation. Note that linear lines are also fitted to the computational results on the basis of the classical Paris equation for comparison purpose.

The effects of the cohesive fracture parameters (ϕ_n, σ_{max}) on the fatigue crack growth rate (da/dN) are investigated with the fixed separation and traction resistance parameters (i.e. $\kappa_n^\Delta = 10$, $\kappa_n^T = 80$). For the effect of the fracture energy, ϕ_n is selected as 700 N/m, 750 N/m and 800 N/m with the cohesive strength of 6.66 MPa. The computational results illustrate that higher fracture energy leads to slower fatigue crack growth rate as shown in Fig. 10(a). Basically, the slope of the $da/dN - \Delta K_I$ curve in the stable fatigue crack growth region decreases with respect to the increase of the fracture energy. For the smaller fracture energy, the stable fatigue crack growth region finishes at the relatively lower stress intensity factor. Next, the cohesive strength (σ_{max}) is selected as 5 MPa, 6.66 MPa and 8 MPa under the constant fracture energy of 800 N/m. Higher cohesive strength results in more resistance on the fatigue crack growth, as expected [Fig. 10(b)]. Therefore, in the proposed fatigue traction-separation relation, both fatigue resistance and cohesive fracture parameters consistently influence the fatigue crack growth rate.

4.3. Modified mixed-mode bending test

A modified mixed-mode bending (MMB) test is simulated to demonstrate fatigue crack growth under mixed-mode loading
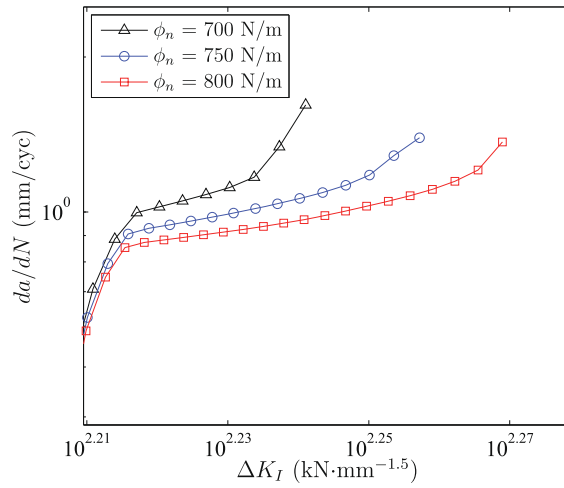
(a)
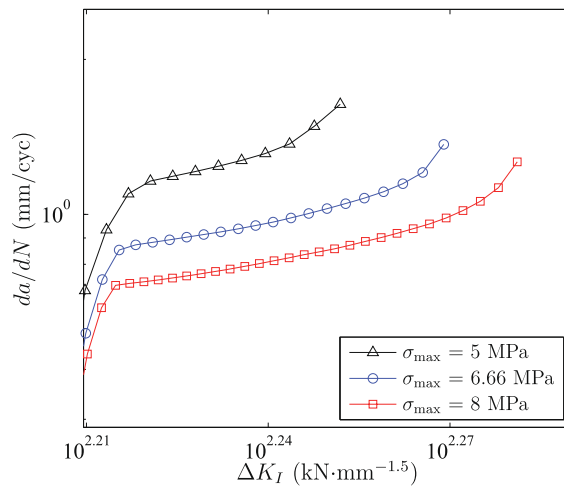
(b)

Fig. 10. Change of the fatigue crack growth rate (a) the fracture energy and (b) the cohesive strength.
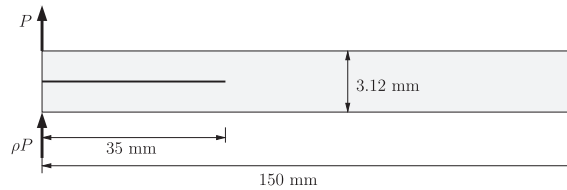

Fig. 11. Geometry and boundary conditions of the modified mixed-mode bending (MMB) test.

condition. The original MMB test was proposed in [35], while a modified MMB configuration was employed to have a constant ratio of the normal to tangential energy release rates during fatigue crack growth [17,19]. The specimen geometry and boundary conditions of the modified MMB test are illustrated in Fig. 11. The fixed displacement boundary condition is applied on the right edge, while cyclic loading is applied at the left-top and -bottom corners with the magnitudes of P and ρP, respectively. The loading ratio (ρ) is selected as 0.07180, which leads to the same strain energy release rate for each mode [52,36,19], i.e.,

$$G_I = G_{II} = \frac{3}{(2 + \sqrt{3})^2} \frac{(Pa)^2}{BEI} \tag{25}$$

where B and I are the beam thickness and the second moment of area, respectively, and E is the elastic modulus.
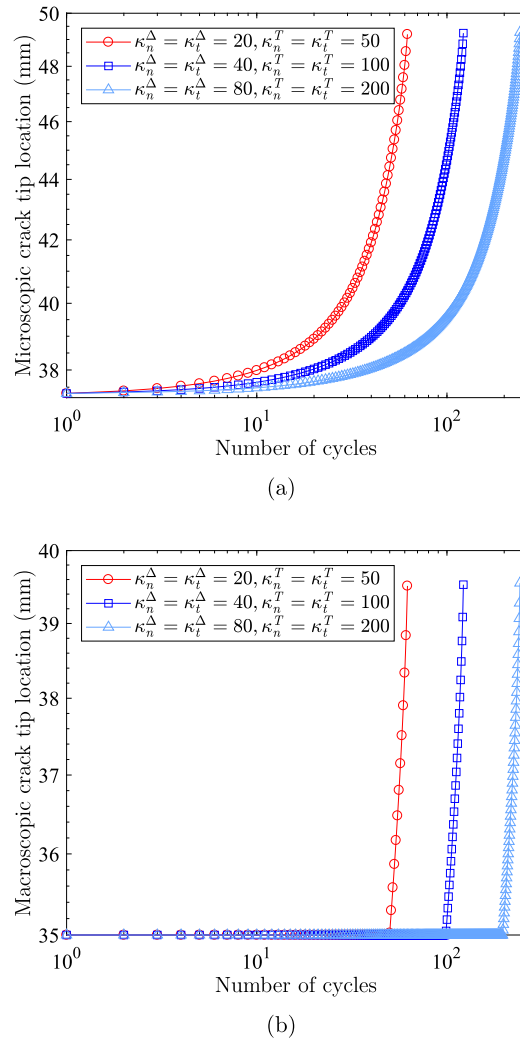
(a)

(b)

Fig. 12. (a) Microscopic and (b) macroscopic crack tip locations according to the variation of the fatigue resistance parameters.

The beam size is 150×3.12 mm with a thickness (B) of 25.4 mm, and the length of an initial notch (a_0) is 35 mm. The maximum and the minimum values of the load (P) are 100 kN and 10 kN, respectively. The material is assumed as isotropic with the elastic modulus of 122 GPa and Poissons ratio of 0.25. Additionally, plane stress condition is assumed for the computational simulation. For the cohesive fracture parameters, the fracture energy (ϕ_n, ϕ_t) and the cohesive strength (σ_{max}, τ_{max}) are selected as 500 N/m and 10 MPa, respectively. The initial slope indicator (λ_n, λ_t) is 0.02, while the shape parameter (α, β) is 3. Three sets of the fatigue resistance parameters (κ_n^Δ, κ_t^Δ, κ_n^T, κ_t^T) are employed in this study, i.e., (1) $\kappa_n^\Delta = \kappa_t^\Delta = 20$ and $\kappa_n^T = \kappa_t^T = 50$, (2) $\kappa_n^\Delta = \kappa_t^\Delta = 40$ and $\kappa_n^T = \kappa_t^T = 100$, and (3) $\kappa_n^\Delta = \kappa_t^\Delta = 80$ and $\kappa_n^T = \kappa_t^T = 200$. The contact separation and traction ratios are assumed to be 0.3 and 0.0, respectively. The domain is discretized using 4-node quadrilateral elements, while the cohesive elements are inserted along the horizontal direction. The number of continuum and cohesive elements are 28500, and 1150, respectively, and the number of nodes is 30776.

For the three sets of the fatigue resistance parameters, the fatigue crack growth of the modified MMB test is investigated. The crack tip location versus the number of loading cycles relations are plotted in Fig. 12. The crack tip location is defined by two different approaches, i.e., microscopic crack tip and macroscopic crack tip. The microscopic crack tip is defined by the critical separation (δ_{nc}, δ_{tc}), while the macroscopic crack tip is determined by the complete separation (δ_n, δ_t). Under mixed mode condition, the microscopic (or macroscopic) crack tip location is where either normal or tangential separation reaches to the normal or tangential critical (or complete) separation, respectively. When the crack tip is defined by the critical separation, i.e., microscopic crack tip, the crack growth is observed from the beginning of the computation [Fig. 12(a)]. If the crack tip location is obtained from the complete separation [Fig. 12(b)], the crack does not propagates up to a certain number of cycles, and then relatively rapid crack growth is observed. As the fatigue resistance parameters increase, the number of required cycles increases, i.e., 50 cycles, 99 cycles, and 197 cycles, for the formation of a macroscopic crack, as expected. The increase of the fatigue resistance parameters leads to slower fatigue crack initiation. Additionally, more cycles are needed for fatigue crack growth according to the higher values of the
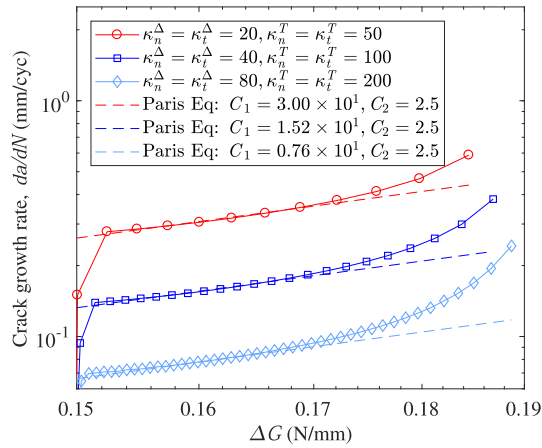
Fig. 13. Fatigue crack growth rate versus strain energy release rate according to the variation of the fatigue resistance parameters.

fatigue resistance parameters, as shown in the previous examples.

Next, the computational results of the fatigue crack growth rate (da/dN) are compared with a modified Paris law according to the energy release rate [51], i.e., $da/dN = C_1(\Delta G)^{C_2}$, where ΔG is the change of the strain energy release rate during each cycle. Then, the relation between the fatigue crack growth rate and the strain energy release rate (e.g., $\Delta G = \sqrt{\Delta G_I^2 + \Delta G_{II}^2}$) is plotted in Fig. 13. Higher values of the fatigue resistance parameter result in slower fatigue crack growth, as expected.

4.4. Three-point bending test

In order to demonstrate the validity of the proposed fatigue crack growth model, a computational result is compared to the fatigue bending experiment performed by Shah and Kishen [44]. The test configuration of a concrete beam is shown in Fig. 14, and a cyclic load is applied to the beam until the complete failure. Note that a cyclic load of 0.5 kN is increased every after 500 cycles while having the constant minimum load of 0.2 kN. In addition, the compressive strength of concrete was 34 MPa, and the peak load under the monotonic loading was measured as 4.46 kN. Because other material properties of concrete are not reported in the paper, they are assumed on the basis of available information (e.g. peak load) and previous literature [38,32]. The elastic modulus and the Poisson's ratio are 21 GPa and 0.25, respectively. For the cohesive fracture parameters, the cohesive strength is 4.6 MPa and the fracture energy is 150 N/m with the shape parameter of 5. In the fatigue traction-separation relation, the fatigue separation and traction resistance parameters are selected as 250 and 1650, respectively, with the contact separation ratio of 0.3 and the zero contact traction ratio.

Both monotonic and cyclic loading cases are simulated. For the monotonic loading case, the peak load of the computational result is 4.46 kN, which corresponds to the experimental result. For the cyclic loading case, the load versus crack mouth opening displacement (CMOD) curves are plotted in every 500 cycles up to 3000 cycles and in every 100 cycles after 3000 cycles including the last cycle before the failure, as shown in Fig. 15(a). The computational and experimental results demonstrate the decrease of the stiffness and the increase of a finite separation at the minimum load during the cyclic loading. The failure of the beam is observed at the 3.5 kN, which is lower than the peak load for the monotonic loading condition. Note that the failure occurs after 3256 cycles in the experiment while it occurs after 3208 cycles in the computation. In addition, the change of the unloading–reloading stiffness is plotted in Fig. 15(b) for both experimental and computational results, which displays good agreement. Note that the unloading–reloading stiffness is simply evaluated by calculating the slope from the minimum loading point to the maximum loading point.

5. Conclusion

A mixed-mode fatigue crack growth model is proposed on the basis of five separation states (softening, unloading, reloading,
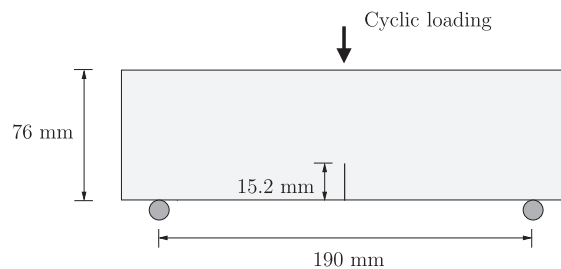

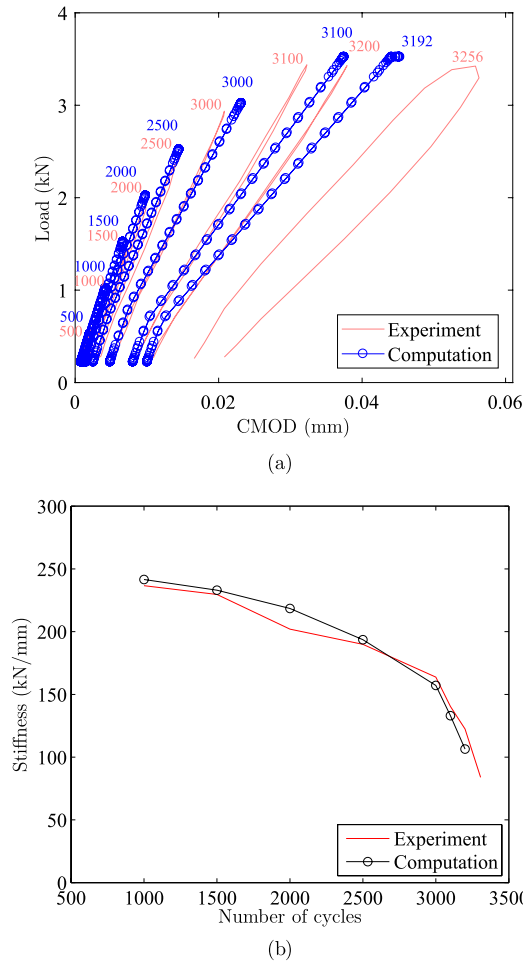**Fig. 14.** Geometry of a three-point bending test.

(a)

(b)

Fig. 15. Comparison between experiments and computational results: (a) load versus crack mouth opening displacement (CMOD) curves, and (b) decrease of the stiffness with respect to the number of cycles.

contact, and complete failure) and damage measures associated with local separation and stress (or traction) states. The separation damage measure (D_n^Δ, D_t^Δ) is proportional to the rate of the separation and inversely proportional to the separation rate resistance parameter (κ_n^Δ, κ_t^Δ). Similarly, the stress (or traction) damage measure (D_n^T, D_t^T) is proportional to the rate of the traction and inversely proportional to the traction rate resistance parameter (κ_n^T, κ_t^T). Because of the stress damage measure, fatigue damage can be accumulated during cyclic loading although cohesive surface elements are not inserted in the domain. Additionally, the contact separation and traction ratios (C_s, C_t) are introduced in order to define the onset of normal contact condition. The proposed model introduces fatigue damage before the local cohesive traction reaches the cohesive strength in the loading history. The effects of the fatigue resistance parameters and the cohesive fracture parameters on the fatigue traction-separation relation and the fatigue crack growth are investigated for both mode-I and mixed-mode examples. The computational results illustrate consistency with respect to the change of the fatigue resistance parameters, fracture energy and cohesive strength. The results also capture stable fatigue crack growth behavior represented by the Paris type relation. The effect of the fracture energy and cohesive strength on fatigue crack growth is investigated, and the fracture properties consistently affect the fatigue crack growth rate. Finally, a fatigue crack growth computation is compared with a three-point bending test of concrete, which demonstrates good agreement between computation and experiment.

For the generalization of the proposed mixed-mode fatigue crack growth model, further in-depth investigation is needed. For example, the present study focuses on low-cycle fatigue examples, and the model is validated for a quasi-brittle material. Additionally, a fatigue crack path is pre-defined, and thus surface elements are inserted along the potential crack path. Some of these constraints should be revisited. Moreover, model parameter calibration is essential to estimate fatigue life of a structure.

Declaration of Competing Interest

The authors declare that they have no known competing financial interests or personal relationships that could have appeared to

influence the work reported in this paper.

Acknowledgements

Appendix A. Supplementary material

Supplementary data associated with this article can be found, in the online version, at https://doi.org/10.1016/j.engfracmech.2020.107234.

References

[1] Abaqus. Analysis User's Manual, Version 6.16. Dassault Systemes Simulia Corp. France: Villacoublay Cedex; 2016.
[2] Abdul-Baqi A, Schreurs P, Geers M. Fatigue damage modeling in solder interconnects using a cohesive zone approach. Int J Solids Struct 2005;42(3):927–42.
[3] Baek H, Park K. Cohesive frictional-contact model for dynamic fracture simulations under compression. Int J Solids Struct 2018;144–145:86–99.
[4] Bak BLV, Sarrado C, Turon A, Costa J. Delamination under fatigue loads in composite laminates: A review on the observed phenomenology and computational methods. Appl Mech Rev 2014;66(6):060803.
[5] Beaurepaire P, Schuëller GI. Modeling of the variability of fatigue crack growth using cohesive zone elements. Eng Fract Mech 2011;78(12):2399–413.
[6] Bouvard JL, Chaboche JL, Feyel F, Gallerneau F. A cohesive zone model for fatigue and creep-fatigue crack growth in single crystal superalloys. Int J Fatigue 2009;31(5):868–79.
[7] Corbani S, Castro J, Miranda A, Martha L, Carter B, Ingraffea A. Crack shape evolution under bending-induced partial closure. Eng Fract Mech 2018;188:493–508.
[8] Davila CG. From s-n to the paris law with a new mixed-mode cohesive fatigue model for delamination in composites. Theoret Appl Fract Mech 2020;106:102499.
[9] de Andres A, Perez JL, Ortiz M. Elastoplastic finite element analysis of three-dimensional fatigue crack growth in Aluminum shafts subjected to axial loading. Int J Solids Struct 1999;36(15):2231–58.
[10] de Moura MFSF, Goncalves JPM. Cohesive zone model for high-cycle fatigue of adhesively bonded joints under mode I loading. Int J Solids Struct 2014;51(5):1123–31.
[11] de Moura MFSF, Goncalves JPM. Cohesive zone model for high-cycle fatigue of composite bonded joints under mixed-mode I+II loading. Eng Fract Mech 2015;140:31–42.
[12] Dekker R, van der Meer F, Maljaars J, Sluys L. A cohesive XFEM model for simulating fatigue crack growth under mixed-mode loading and overloading. Int J Numer Meth Eng 2019;118(10):561–77.
[13] Deshpande VS, Needleman A, Van der Giessen E. A discrete dislocation analysis of near-threshold fatigue crack growth. Acta Mater 2001;49(16):3189–203.
[14] Dodds Jr. RH, Carlyle AG. Three-dimensional effects on fatigue crack closure under fully-reversed loading. Eng Fract Mech 2007;74(3):457–66.
[15] Foote RML, Buchwald VT. An exact solution for the stress intensity factor for a double cantilever beam. Int J Fract 1985;29:125–34.
[16] Ghovanlou MK, Jahed H, Khajepour A. Cohesive zone modeling of fatigue crack growth in brazed joints. Eng Fract Mech 2014;120:43–59.
[17] Harper PW, Hallett SR. A fatigue degradation law for cohesive interface elements – Development and application to composite materials. Int J Fatigue 2010;32(11):1774–87.
[18] Jha D, Banerjee A. A cohesive model for fatigue failure in complex stress-states. Int J Fatigue 2012;36(1):155–62.
[19] Jimenez S, Liu X, Duddu R, Waisman H. A discrete damage zone model for mixed-mode delamination of composites under high-cycle fatigue. Int J Fract 2014;190(1–2):53–74.
[20] Khoramishad H, Crocombe AD, Katnam KB, Ashcroft IA. Predicting fatigue damage in adhesively bonded joints using a cohesive zone model. Int J Fatigue 2010;32(7):1146–58.
[21] Li H, Yuan H, Li X. Assessment of low cycle fatigue crack growth under mixed-mode loading conditions by using a cohesive zone model. Int J Fatigue 2015;75:39–50.
[22] Maiti S, Geubelle PH. A cohesive model for fatigue failure of polymers. Eng Fract Mech 2005;72(5):691–708.
[23] Maiti S, Geubelle PH. Cohesive modeling of fatigue crack retardation in polymers: Crack closure effect. Eng Fract Mech 2006;73(1):22–41.
[24] Miranda ACO, Gerlich A, Walbridge S. Aluminum friction stir welds: Review of fatigue parameter data and probabilistic fracture mechanics analysis. Eng Fract Mech 2015;147:243–60.
[25] Newman JC. A crack opening stress equation for fatigue crack growth. Int J Fract 1984;24(4):R131–5.
[26] Nguyen O, Repetto EA, Ortiz M, Radovitzky RA. A cohesive model of fatigue crack growth. Int J Fract 2001;110(4):351–69.
[27] Nojavan S, Schesser D, Yang QD. A two-dimensional in situ fatigue cohesive zone model for crack propagation in composites under cyclic loading. Int J Fatigue 2016;82:449–61.
[28] Paris PC, Erdogan F. A critical analysis of crack propagation laws. J Basic Eng - ASME 1963;85:528–34.
[29] Park K, Choi H, Paulino GH. Assessment of cohesive traction-separation relationships in ABAQUS: A comparative study. Mech Res Commun 2016;78:71–8.
[30] Park K, Paulino GH. Computational implementation of the PPR potential-based cohesive model in ABAQUS: Educational perspective. Eng Fract Mech 2012;93:239–62.
[31] Park K, Paulino GH. Cohesive zone models: A critical review of traction-separation relationships across fracture surfaces. Appl Mech Rev 2013;64(6):060802-1–060802-20.
[32] Park K, Paulino GH, Roesler JR. Determination of the kink point in the bilinear softening model for concrete. Eng Fract Mech 2008;75(13):3806–18.
[33] Park K, Paulino GH, Roesler JR. A unified potential-based cohesive model of mixed-mode fracture. J Mech Phys Solids 2009;57(6):891–908.
[34] Qian J, Fatemi A. Mixed mode fatigue crack growth: A literature survey. Eng Fract Mech 1996;55(6):969–90.
[35] Reeder JR, Crews Jr. JH. Mixed-mode bending method for delamination testing. AIAA J 1990;28(7):1270–6.
[36] Robinson P, Galvanetto U, Tumino D, Bellucci G, Violeau D. Numerical simulation of fatigue-driven delamination using interface elements. Int J Numer Meth Eng 2005;63:1824–48.
[37] Roe KL, Siegmund T. An irreversible cohesive zone model for interface fatigue crack growth simulation. Eng Fract Mech 2003;70(2):209–32.
[38] Roesler J, Paulino GH, Park K, Gaedicke C. Concrete fracture prediction using bilinear softening. Cem Concr Compos 2007;29(4):300–12.

[39] Roth S, Hutter G, Kuna M. Simulation of fatigue crack growth with a cyclic cohesive zone model. Int J Fract 2014;188(1):23–45.
[40] Roth S, Kuna M. Prediction of size-dependent fatigue failure modes by means of a cyclic cohesive zone model. Int J Fatigue 2017;100:58–67.
[41] Roychowdhury S, Dodds Jr. RH. Three-dimensional effects on fatigue crack closure in the small-scale yielding regime - a finite element study. Fatigue Fract Eng Mater Struct 2003;26(8):663–73.
[42] Salih S, Davey K, Zou Z. Frequency-dependent cohesive-zone model for fatigue. Int J Solids Struct 2018;152–153:228–37.
[43] Serebrinsky S, Ortiz M. A hysteretic cohesive-law model of fatigue-crack nucleation. Scripta Mater 2005;53(10):1193–6.
[44] Shah SG, Kishen JMC. Use of acoustic emissions in flexural fatigue crack growth studies on concrete. Eng Fract Mech 2012;87:36–47.
[45] Sih GC, Barthelemy BM. Mixed mode fatigue crack growth predictions. Eng Fract Mech 1980;13(3):439–51.
[46] Spring DW, Giraldo-Londono O, Paulino GH. A study on the thermodynamic consistency of the Park-Paulino-Roesler (PPR) cohesive fracture model. Mech Res Commun 2016;78:100–9.
[47] Turon A, Costa J, Camanho PP, Davila CG. Simulation of delamination in composites under high-cycle fatigue. Compos Part A: Appl Sci Manuf 2007;38:2270–82.
[48] Tvergaard V. On fatigue crack growth in ductile materials by crack-tip blunting. J Mech Phys Solids 2004;52(9):2149–66.
[49] Ural A, Heber G, Wawrzynek PA, Ingraffea AR, Lewicki DG, Neto JB. Three-dimensional, parallel, finite element simulation of fatigue crack growth in a spiral bevel pinion gear. Eng Fract Mech 2005;72(8):1148–70.
[50] Ural A, Krishnan VR, Papoulia KD. A cohesive zone model for fatigue crack growth allowing for crack retardation. Int J Solids Struct 2009;46(11–12):2453–62.
[51] Wilkins DJ, Eisenmann JR, Camin RA, Margolis WS, Benson RA. Characterizing delamination growth in graphite-epoxy. In: Reifsnider KL, editor. Damage in Composite Materials, ASTM STP 775. American Society for Testing and Materials; 1982. p. 168–83.
[52] Williams JG. On the calculation of energy release rates for cracked laminates. Int J Fract 1988;36:101–19.
[53] Xu XP, Needleman A. Numerical simulations of fast crack growth in brittle solids. J Mech Phys Solids 1994;42(9):1397–434.
[54] Yuan H, Li X. Critical remarks to cohesive zone modeling for three-dimensional elastoplastic fatigue crack propagation. Eng Fract Mech 2018;202:311–31.
[55] Zerbst U, Vormwald M, Pippan R, Gänser H-P, Sarrazin-Baudoux C, Madia M. About the fatigue crack propagation threshold of metals as a design criterion - A review. Eng Fract Mech 2016;153:190–243.
[56] Ha K, Baek H, Park K. Convergence of fracture process zone size in cohesive zone modeling. Appl Math Model 2015;39:5828–36.